In-situ formation of Ti-Mo biomaterials by selective laser melting of Ti/Mo and Ti/Mo_2C powder mixtures: A comparative study on microstructure, mechanical and wear performance, and thermal mechanisms

Qimin Shi[1], Shoufeng Yang[2]*, Yi Sun[1]*, Yifei Gu[1], Ben Mercelis[3], Shengping Zhong[1], Bart Van Meerbeek[3], Constantinus Politis[1]

1. KU Leuven, Department of Biomedical Sciences, OMFS-IMPATH Research Group & UZ Leuven (University Hospitals Leuven), Oral and Maxillofacial Surgery, Kapucijnenvoer 33, Leuven 3000, Belgium

2. University of Southampton, Faculty of Engineering and Physical Sciences, Southampton SO17 1BJ, UK

3. KU Leuven, Department of Oral Health Sciences, BIOMAT-Biomaterials Research Group & UZ Leuven (University Hospitals Leuven), Dentistry, Kapucijnenvoer 7, Leuven 3000, Belgium

*Corresponding authors.

Email addresses: shoufeng.yang@gmail.com (S. Yang); yi.sun@uzleuven.be (Y. Sun).

Abstract: Ti-Mo alloys/composites are expected to be the next-generation implant material with low modulus but without toxic/allergic elements. However, synthesis mechanisms of Ti-Mo biomaterials in Selective Laser Melting (SLM) vary according to raw materials and fundamentally influence material performance, due to its inhomogeneous chemical composition and stability. Therefore, this work provides a comparative study on the microstructure, mechanical and wear performance, and underlying thermal mechanisms of two promising Ti-Mo biomaterials prepared by SLM but through different synthesis mechanisms to offer scientific understanding for the creation of ideal metal implants. They are (i) Ti-7.5Mo alloys, prepared from a conventional Ti/Mo powder mixture, and (ii) Ti-7.5Mo-2.4TiC composites, in-situ prepared from Ti/Mo_2C powder mixture. Results reveal that the in-situ Ti-7.5Mo-2.4TiC composites made from Ti/Mo_2C powder mixture by SLM can produce 61.4% more β phase and extra TiC precipitates (diameter below 229.6 nm) than Ti-7.5Mo alloys. The fine TiC not only contributes to thinner and shorter β columnar grains under a large temperature gradient of 51.2 K/μm but also benefits material performance. The in-situ Ti-7.5Mo-2.4TiC composites produce higher yield strength (980.1 ± 29.8 MPa) and ultimate compressive strength (1561.4 ± 39 MPa) than the Ti-7.5Mo alloys, increasing by up to 12.1%. However, fine TiC and its aspect ratio (2.71) dominate an unfavourable rise of elastic modulus to 91.9 ± 2 GPa, 44.7% higher than Ti-7.5Mo alloys, which, nevertheless, is still lower than the modulus of traditional Ti-6Al-4V. While, TiC and its homogeneous distribution benefit wear resistance, decreasing the wear rate of the in-situ Ti-7.5Mo-2.4TiC composites to 6.98×10^{-4} $mm^3N^{-1}m^{-1}$, which is 36% lower than that of Ti-7.5Mo alloys. Therefore, although with higher modulus than the Ti-7.5Mo alloys, the SLM-fabricated in-situ Ti-7.5Mo-2.4TiC composites can expect to provide good biomedical application potential in cases where combined good strength and wear resistance are required.

Keywords: Selective laser melting (SLM); Titanium; Metal matrix composites; Microstructures; Mechanical properties; Wear properties

1. Introduction

Selective Laser Melting (SLM), as a promising branch of laser additive manufacturing technique, is providing an ideal platform to create patient-specific, customised orthopaedic implants that are not achievable with conventional manufacturing routes [1-4]. These customised biomedical devices show higher potential to reduce the time for surgery, recovery and rehabilitation, reconstruct joint kinetics, enhance implant fixation, and lower the necessity to conduct revision surgery, due to the significantly improved geometrical match between the implant structure and the patient's anatomy, compared to those off-the-shelf orthopaedic implants [5].

Titanium (Ti)-based alloys are considered ideal candidates as implant materials due to their low density, low elastic modulus, good bio-corrosion resistance and mechanical properties, and high biocompatibility [1]. The traditional biomedical Ti-based alloys, such as the commonly used Ti-6Al-4V (elastic modulus of around 110 GPa), have much lower elastic moduli than 316LSS (210 GPa) and Co-Cr alloys (240 GPa). Nevertheless, their elastic moduli are still higher than that of human bone (10-30 GPa). According to Wolff's law [6], stress shielding on a bone can be caused due to the modulus mismatch between the metal orthopaedic implant and the surrounding bone, eventually resulting in loss of bone density, which is revealed as one of the fundamental reasons for implant loosening clinically. Another concern of Ti-6Al-4V is its unfavourable relation to Alzheimer's diseases and anaphylaxis induced by the alloying addition of Aluminum (Al) and Vanadium (V). Clinical studies [7] revealed that Al is neurotoxic and could play a role in the establishment of Alzheimer's disease by causing the formation of neurofibrillary tangles and characteristic beta-amyloid. Cell culture studies [8] evidenced that V has the capability to induce genotoxic lesions, anti-apoptotic effects and cell morphological transformation in certain types of human cells. Therefore, developing low-modulus Ti-based materials without toxic and allergic elements can greatly benefit future implant applications. Among them, Titanium-Molybdenum (Ti-Mo) alloys are the representative ones given that the non-toxic and non-allergenic Mo can be an effective β stabiliser to design Ti-based alloys with a β structure that usually has a lower modulus than the α phase [9-11].

In general, two material synthesis routes can be accessible to prepare Ti-Mo alloys (or composites). The conventional one starts from pure Mo and Ti components by, for instance, powder metallurgy [12], arc-melting furnace [13], casting [14], etc. Recently, an in-situ synthesis mechanism is being practised to prepare Ti-Mo composites strengthened by extra precipitated ceramic reinforcements [15], to meet the increasing demand for improved wear resistance in the clinic. Many clinical cases have reported that their success rates are significantly restricted by insufficient wear resistance, since the wear debris of Ti is possible to activate pro-inflammatory cytokines, including IL1β, (TNF)-α, and IL6, leaving undesirable osteolytic events [16]. A good example of the in-situ synthesis of Ti-Mo composites is to replace Mo with Molybdenum Carbide (Mo_2C) as raw material to achieve a Ti-Mo matrix reinforced by precipitated TiC particles, forming Ceramic Particle Reinforced Metal Matrix Composites (CPRMMCs) [17].

Compared to using the pre-alloyed powder to prepare Ti-Mo alloys/composites by SLM, using powder mixtures can be more flexible to adjust the chemical compositions within the powder mixture [18]. Powder mixtures have been widely used in SLM to prepare metal-based alloys and composites [18-20]. Their results show that although local chemical segregation can happen, different powder components can be mixed well with a good macro homogeneity to achieve ideal mechanical properties. The synthesis mechanism starting from the Ti/Mo and Ti/Mo_2C powder mixture determines the property of materials in a different manner. With the absorption of laser energy via powder-coupling and bulk-coupling mechanisms during SLM [21], Ti and Mo or Ti and Mo_2C powder within the molten pool can be (partially) melted and decomposed into free chemical elements (Ti, Mo and C). Zhang et al. [11] have reported that the basic α and β phase in the Ti-Mo system show high sensitivity to the Mo content. Therefore, the introduction of β stabiliser Mo can substantially lower the β→α transus temperature, leaving more low-modulus β phase to the Ti-Mo biomaterials. Differently, the extra heat from the in-situ exothermic Ti/Mo_2C reaction may accelerate the decomposition of Mo_2C and diffusion of Mo into the Ti matrix [22], probably retaining more β phase, which is beneficial for biomaterials where low-modulus β phase is required. However, considering the higher modulus of ceramics, the precipitated product, TiC, may cause an unfavourable increase of the elastic modulus of the composites.

On the other hand, the size and shape of precipitated TiC particles and their distribution state in the Ti matrix can exert extra influence on the mechanical property and even the failure mode of the in-situ Ti-Mo-TiC composites. Fine TiC particles contribute to a higher surface-to-volume ratio of the reinforcements, strengthening the ceramic/matrix interface and eventually achieving higher mechanical properties of the CPRMMCs [23]. What's more, the precipitation of TiC benefits wear properties considering the good wear resistance of ceramics. However, the agglomeration of fine particles driven by Van Der Waals attractive force could significantly lower composites' mechanical performance, due to the crack initiation and propagation starting from the particle clusters [24]. Therefore, taking advantage of the in-situ Ti/Mo_2C reaction to achieve a low modulus and high wear resistance while avoiding TiC agglomeration becomes a critical issue for SLM of Ti-Mo composites.

In this case, having a thorough understanding of the thermophysical, chemical and metallurgical behaviours behind the two Ti-Mo synthesis mechanisms by SLM can be necessary to produce Ti-Mo biomaterials with ideal mechanical and wear properties. Up to date, SLM of Ti-Mo alloys has been practised [25, 26], while the synthesis of Ti-Mo composites through the in-situ Ti/Mo_2C synthesis mechanism by SLM has less been studied. As a result, the comparison and exploration of the two different synthesis routes to produce Ti-Mo biomaterials by SLM can barely be found. Although Vrancken et al. [17] practised SLM of Ti-Mo-TiC metal matrix composites initiating from a powder mixture including Ti, Mo and Mo_2C, the addition of Mo together with Mo_2C seems to make it ambiguous to understand the different roles of these two components in the Ti-Mo composites.

In this work, a comparative study was conducted to investigate the microstructure, mechanical and wear properties of the Ti-Mo biomaterials prepared by SLM using Ti/Mo and Ti/Mo_2C powder mixture, respectively. The underlying thermal mechanisms behind the metallurgical differences were further explored by performing a numerical simulation of thermal conductive behaviours during the SLM. Considering the introduction of 7.5 wt% Mo into the Ti matrix has high potential to achieve a low modulus with balanced mechanical properties in Ti-Mo system material, as revealed by various material processing routes, including casting [14] and SLM process [26], this work started from two groups of powder mixtures: (1) 7.5 wt% Mo + remainder CP Ti (termed as Ti-7.5Mo), and (2) 8.0 wt% Mo_2C + remainder CP Ti. The powder mixing ratio of Ti/Mo_2C was settled to theoretically fulfil the in-situ reaction Ti-8Mo_2C→Ti-7.5Mo-2.4TiC so that the two material groups own the same theoretical Mo content. Therefore, the second biomaterial is termed as in-situ Ti-7.5Mo-2.4TiC composites. The objective of this work was to fundamentally understand the critical metallurgical and thermal mechanisms of the Ti-Mo biomaterials prepared by SLM using different synthesis routes and their influence on mechanical and wear properties.

2. Experiments and numerical simulation

2.1 Powder preparation

Spherical gas-atomised CP Ti powder (grade 1), with a particle size distribution of 10-45 μm and an average diameter of 30 μm, was supplied by LPW Technology, UK. The chemical composition of CP Ti is ≤ 0.20 Fe, ≤ 0.12 O, ≤ 0.08 C, ≤ 0.01 H, ≤ 0.02 N and Ti balance (wt%). Mo (particle size of 3-5 μm; Beijing Xingrongyuan Technology Co., Ltd., China) and Mo_2C (particle size of 3-5 μm; Hunan WISE New Material Technology Co., Ltd., China) powders were added as reinforcements into the two powder mixtures, respectively. The chemical composition of Mo powder is < 0.005 Fe, < 0.001 Si, < 0.001 Al, < 0.03 C, 0.001 N, < 0.15 O, < 0.001 S+P and Mo balance (wt%). The chemical composition of Mo_2C powder is ≥ 5.85 total carbon, ≤ 0.20 free carbon, ≤ 0.01 Nb, ≤ 0.05 Fe, ≤ 0.05 Si, ≤ 0.50 O, ≤ 0.10 N, ≤ 0.01 Na, ≤ 0.005 K, ≤ 0.01 Ca and Mo balance (wt%). Two groups of powder mixture — 7.5 wt% Mo + remainder CP Ti, and 8.0 wt% Mo_2C + remainder CP Ti — were dry mixed for 24 hours in a Turbula mixer, respectively, to achieve homogeneous mixing among powder components (Fig. 1(a) and 1(b)). Although slightly agglomerated Mo or Mo_2C additions were observed in the powder mixture, the spherical morphology of the Ti powder was well protected after the powder mixing process. Considering the comparatively low content of Mo and Mo_2C components within the powder mixture, the spherical Ti powder can expect to guarantee the good flowability of the powder mixture during SLM [27, 28].

2.2 SLM process

An in-house developed SLM machine with an IPG Photonics Ytterbium YLR-500-WC fibre laser (producing a 1060 nm wavelength in continuous mode and a 50 μm spot diameter) was employed to prepare specimens of 10 mm × 10 mm × 8 mm (Length × Width × Height), using a 90° bidirectional island scanning strategy (Fig. 1(c)). After preliminary SLM experiments on the SLM machine, two groups of specimens were produced both under a laser power of 220 W, a powder bed thickness of 30 μm and a hatch space of 70 μm. However, Ti-7.5Mo alloys used a slightly faster laser scanning speed (1200 mm/s) than the in-situ Ti-7.5Mo-2.4TiC composites (1100 mm/s). The slower laser scanning speed used in the Ti/Mo_2C powder mixture can be ascribed to the relatively low thermal conductivity of Mo_2C powder, lowering the thermal conductivity of the powder mixture. As to reach the necessary molten pool size to realise metallurgical bonding between adjacent powder layers, a higher laser energy input, by lowering the laser scanning speed if other laser parameters keep the same, is required in the Ti/Mo_2C powder mixture to guarantee sufficient heat conducted from the top surface of the powder bed to the bottom. The prepared specimens have flat and dense top surfaces with fine solidification ripples reflecting the smooth flow behaviour of metal liquid during SLM (Fig. 1(d-f)). Taking these features together can further suggest the good flowability of the powder mixture in this work.

The chemical composition of light elements, such as oxygen (O) and nitrogen (N), can influence the mechanical properties of the Ti components due to the α-stabilising effect by these interstitial atoms [29]. On the other hand, these light elements can dissolve into the Ti matrix and are strong solid solution strengtheners to improve the mechanical properties of the Ti components [30]. Therefore, to minimise the extra effect of these light elements contamination on mechanical properties in this study, the SLM chamber atmosphere was strictly controlled during the specimen preparation process. Firstly, the chamber was vacuumed to remove the gas inside. Then, high-purity argon gas (99.999%) was introduced to refill the chamber, making the air pressure inside the chamber slightly higher than the outside air pressure to prevent outside gas containing O, N and C from intruding into the SLM chamber. The argon gas was injected continuously to guarantee the whole SLM process was done under the oxygen concentration below 0.01%.

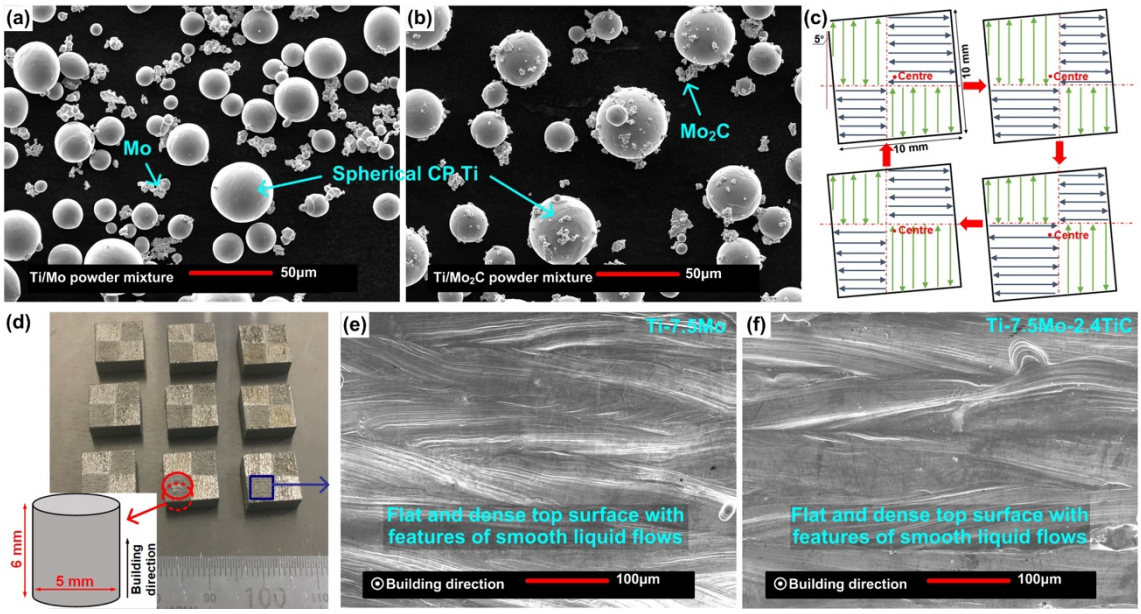

Fig. 1. (a) Ti/Mo powder mixture, (b) Ti/Mo_2C powder mixture, (c) island laser scanning strategy applied during SLM, (d) prepared specimens with flat and dense top surfaces on (e) SLM-fabricated Ti-7.5Mo alloys and (f) in-situ Ti-7.5Mo-2.4TiC composites.

2.3 Characterisation of microstructures and chemical compositions

The relative density was measured by Archimedes' principle. The preliminary optical microscope (OM) observation was performed on an inverted light optical microscope Leica DM ILM. The scanning electron microscope (SEM) characterisation using back-scattered electron (BSE) and secondary electron (SE) mode, and the chemical composition analysis were performed on a Philips XL30 FEG, Eindhoven, Netherlands, equipped with an energy dispersive spectrometer (EDS; EDAX Inc., USA). Material phases were identified by a Seifert 3003 T/T X-ray diffractometer (XRD) with a Cu Kα radiation (λ = 0.1543 nm) under 40 kV and 40 mA. A step-scan type was used at a range of 2θ = 30-80º (step width = 0.02º, exposure time for each step = 1s). The specimen for XRD and SEM was grounded and polished, following the standard procedures for metallographic observations. The specimen was etched using a solution including 6 mL HNO_3, 3 mL HF, and 100 mL distilled water for twenty seconds for microstructural observation.

Quantitative analysis of the major phases in the Ti-7.5Mo alloys and Ti-7.5Mo-2.4TiC composites was performed using a Reference Intensity Ratio (RIR) method by comparing strongest peaks intensities [31]. K_x, representing the RIR value of a certain phase x, is calculated as I_x/I_c. I_x is the intensity of 100% peak of phase x, and I_c is the intensity of 100% peak of the mixture of phase x and corundum (Al_2O_3, standard materials) in 50:50 by weight, respectively. RIR values of α-Ti and β-Ti are provided in the PDF cards. Considering the low contents of minor phases including residual Mo and Mo_2C and precipitated TiC in the material, the Ti-7.5Mo alloys and Ti-7.5Mo-2.4TiC composites are mainly composed of α and β phase, as revealed in XRD patterns. Therefore, the weight fraction of α (W_α) and β (W_β) phase can be calculated by:

$$W_\alpha = I_\alpha / (I_\alpha + I_\beta \cdot K_{\alpha/\beta}) \quad (1)$$

$$W_\beta = I_\beta / (I_\beta + I_\alpha \cdot K_{\alpha/\beta}) \quad (2)$$

$$K_{\alpha/\beta} = K_{\alpha}/ K_{\beta} \quad (3)$$

where $K_{\alpha} = I_{\alpha}/I_{c}$ = 6.44, PDF#89-3725; $K_{\beta} = I_{\beta}/I_{c}$ = 9.61, PDF#89-4913.

2.4 Numerical simulation of thermal behaviours

Numerical simulations reflecting the SLM experimental process were performed on an ANSYS platform using the processing parameters in the SLM experiments to explore the thermophysical mechanism behind the microstructural development. A 3D finite element model consisting of a Ti/Mo or Ti/Mo_2C powder bed with two layers (Width 1050 μm × Length 1050 μm × Thickness 30 μm × 2 layers) and a Ti-6Al-4V substrate (Width 1700 μm × Length 1700 μm × Height 300 μm) was established (Fig. 2). Point 1 at the centre of a laser scanning island on the second powder layer was monitored to determine the molten pool size and internal thermal behaviours. The powder bed was meshed by fine ANSYS Solid 70 hexahedron units (element size of Width 8.75 μm × Length 8.75 μm × Height 7.5 μm), and the Ti-6Al-4V substrate was meshed by relatively coarse tetrahedron units, producing 161,080 nodes and 326,428 elements in total. The temperature-dependent thermal conductivity ($k_{s\text{-}bulk}$), heat capacity ($C_{P\text{-}bulk}$), density (ρ_{Bulk}), and melting temperature (T_M) of the bulk material, as well as the laser absorptivities (A) of the powder, are summarised in Table 1. The temperature governing equation, initial and boundary condition, design of moving Gaussian heat source, latent heat during phase change (including the reaction exotherm of in-situ Ti/Mo_2C), and determination of thermophysical parameters for powder mixtures consulted the literature [32-34] and are described in the supplementary material. To reflect the in-situ Ti/Mo_2C reaction during SLM, the thermophysical properties of Ti/Mo_2C powder mixture was assigned before 873 K (at which point the in-situ Ti/Mo_2C reaction was ignited, reaching Ti-7.5Mo-2.4TiC [22]), and thermophysical properties of Ti-7.5Mo-2.4TiC were loaded after 873 K.

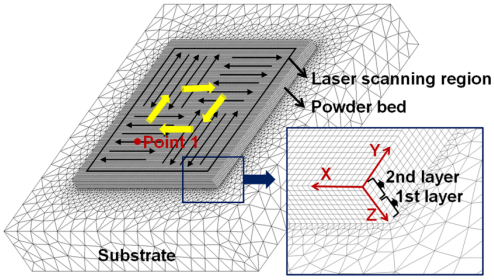

Fig. 2. Three-dimensional finite element model during numerical simulation.

Table 1 Thermophysical parameters of CP Ti [34], Mo [35], Mo_2C and TiC [32, 36].

Thermal conductivity ($k_{s\text{-}bulk}$) [W/(m·K)]									
Ti [at certain temperatures/K]	21.8 [293]	19.9 [473]	18.6 [673]	20 [873]	21.1 [1073]	22.6 [1273]	24.3 [1473]	26 [1673]	27.8 [1873]
Mo: 139			Mo_2C: 20.92				TiC: 23		
Heat capacity ($C_{P\text{-}bulk}$) [J/(Kg·K)]									
Ti [at certain temperatures/K]	520 [293]	560 [473]	610 [673]	660 [873]	710 [1073]	620 [1273]	650 [1473]	745 [1673]	900 [1873]
Mo: 250			Mo_2C: 347				TiC: 543		
Density (ρ_{Bulk}) [Kg/m^3]									
Ti: 4540		Mo: 10200			Mo_2C: 9180			TiC: 4910	
Melting temperature (T_M) [K]									
Ti: 1933		Mo: 2873			Mo_2C: 2960			TiC: 3340	
Laser absorptivity of powder (A) [%]									
Ti: 77		Mo: 34			Mo_2C: 80			TiC: 82	

2.5. Characterisation of mechanical and wear properties

Microhardness was determined by an FV-700 microhardness tester (Future-Tech Corp., Tokyo, Japan) using a 1 Kg load during 15 s. The final microhardness was from the average of at least ten indentations. Compression tests were performed by an Instron 4467 testing facility at a constant compression rate (0.2 mm/min) with three repetitions for each group of material. Cylindrical compression specimens (diameter = 5 mm and height = 6 mm) were cut from the cube specimen along the building direction (Fig. 1(d)). The specimen surface was ground before the test. The fracture surface was observed by the Philips XL30 FEG.

Room-temperature dry unidirectional sliding wear tests were executed on the bottom plane of the specimen using a pin/ball-mode sliding tester (CS-4.8, SD Mechatronik, Munich, Germany). Before the test, the bottom surface was ground and polished until reaching surface roughness (arithmetic mean deviation) R_a of around 0.047 μm (Fig. 3(a) and 3(b)). A Formtracer CS-3200 profilometer was used to measure the surface roughness, by following ISO 1997 standard. The surface roughness measurements were implemented in five segments totalling a cut-off length of 6.25 mm. The roughness profiles were measured five times to reduce experimental error. During the wear test, SiN ceramic balls with a diameter of 4.763 mm were taken as the counterpart material. Through the synergic movement between the ceramic ball and the specimen mounted on a testing chamber, a sliding path length (L) of 5 mm and a test cycle of 2000 times were achieved (Fig. 3(c)). The test loading ($G_{Loading}$) was constant to be 9.8 N, and the lowest position of the ceramic ball in the Z direction during each test cycle was recorded in real-time. The difference between the lowest ceramic ball position at the first and last cycle reflects the wear scar depth (ΔZ). The worn surface and wear scar width (W) were observed using a JEOL JSM-6610LV SEM. The wear volume (V_W) of the specimen is decided by:

$$V_W = SL \tag{4}$$

where S is the cross-sectional area of the wear scar and is calculated geometrically by:

$$S = R^2\theta/2 - W(R - \Delta Z)/2 \tag{5}$$

where R is the ceramic ball radius, θ is the intersection angle corresponding to the wear scar width and is defined by:

$$\theta = 2\arctan[(W/2)/(R-\Delta Z)] \quad (6)$$

The wear rate (ω_{Wear}) is determined by:

$$\omega_{Wear} = V_W/(2000G_{Loading}L) \quad (7)$$

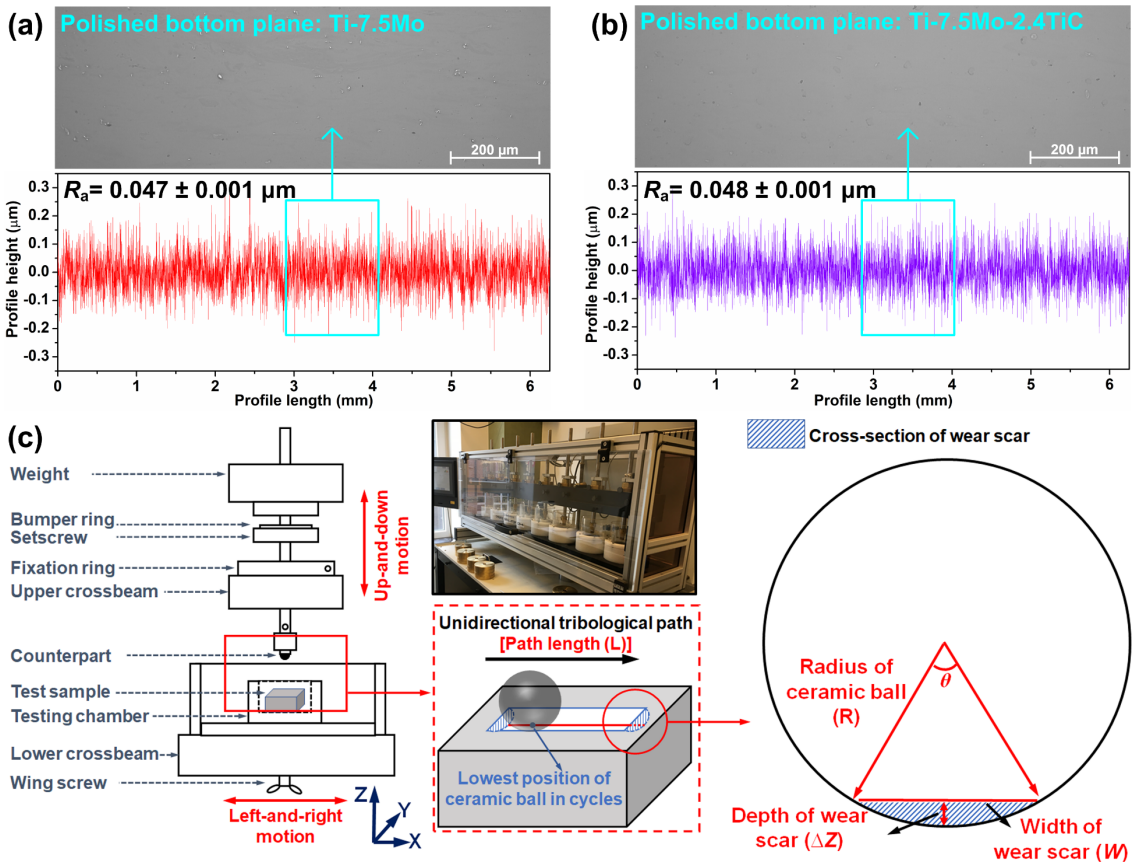

Fig. 3. Roughness profiles on the polished bottom surface of SLM-fabricated (a) Ti-7.5Mo alloys and (b) in-situ Ti-7.5Mo-2.4TiC composites, and (c) schematic of sliding tests.

3. Results and discussion

3.1 Chemical homogeneity within Ti-7.5Mo alloys and in-situ Ti-7.5Mo-2.4TiC composites

Polished cross-sections of the SLM-fabricated Ti-7.5Mo alloys and in-situ Ti-7.5Mo-2.4TiC composites are shown in Fig. 4. In general, specimens show almost fully dense and crack-free, which is corresponding to their high relative densities (Ti-7.5Mo alloys of 99.83 ± 0.05 %, and in-situ Ti-7.5Mo-2.4TiC composites of 99.86 ± 0.05 %). Residual Mo or Mo_2C particles (white contrast) can be seen. Some Mo particles even agglomerate together to form clusters (Fig. 4(a)). In contrast, fewer residual Mo_2C particles are seen in the in-situ Ti-7.5Mo-2.4TiC composites (Fig. 4(d)), which could be attributed to (i) the smaller total Mo_2C volume provided initially in the Ti/Mo_2C powder mixture although with the equivalent Mo weight content (1.99 vol% of Mo_2C in Ti/Mo_2C powder mixture vs 3.90 vol% of Mo in Ti/Mo powder mixture) and the in-situ Ti/Mo_2C exothermic reaction accelerating the decomposition of Mo_2C and diffusion of Mo. Closer observation shows strong colour contrast variation in the Ti-7.5Mo alloys, showing Mo-rich (light-grey contrast) and Mo-poor (dark-grey contrast) streaks (Fig. 4(b)). Such heterogeneous distribution of Mo and Ti is further evidenced by EDS maps (Fig. 4(c)). EDS point analyses determine that the light-grey streaks (Point 1) contain up to

20.62 wt% Mo, while the dark-grey ones only contain 0.57 wt% Mo (Point 2), with an average Mo value of 6.14 wt% across the Ti matrix. Interestingly, the Mo-rich streaks were driven by metallic liquid flows and outlined the molten pool configuration due to the high density of Mo. Kang et al. [25, 26] termed such a meso-scaled two-phase mixed feature as a conchoidal structure, and it contributes to a low elastic modulus and good ductility. The chemical element distribution across a residual particle shows a gradual variation of material compositions at the Ti/Mo interface, confirming the partially molten state of residual alloying additions (see the EDS line in Fig. 4(c)). In contrast, the in-situ Ti-7.5Mo-2.4TiC composites show weaker colour contrast variation in Fig. 4(e) and the comparatively homogeneous Mo, Ti and C across the Ti matrix in Fig. 4(f), indicating a relatively complete mixing between Mo and Ti. As a result, the average Mo content (7.06 wt%) in the Ti matrix is increased by 15% compared to the Ti-7.5Mo alloys.

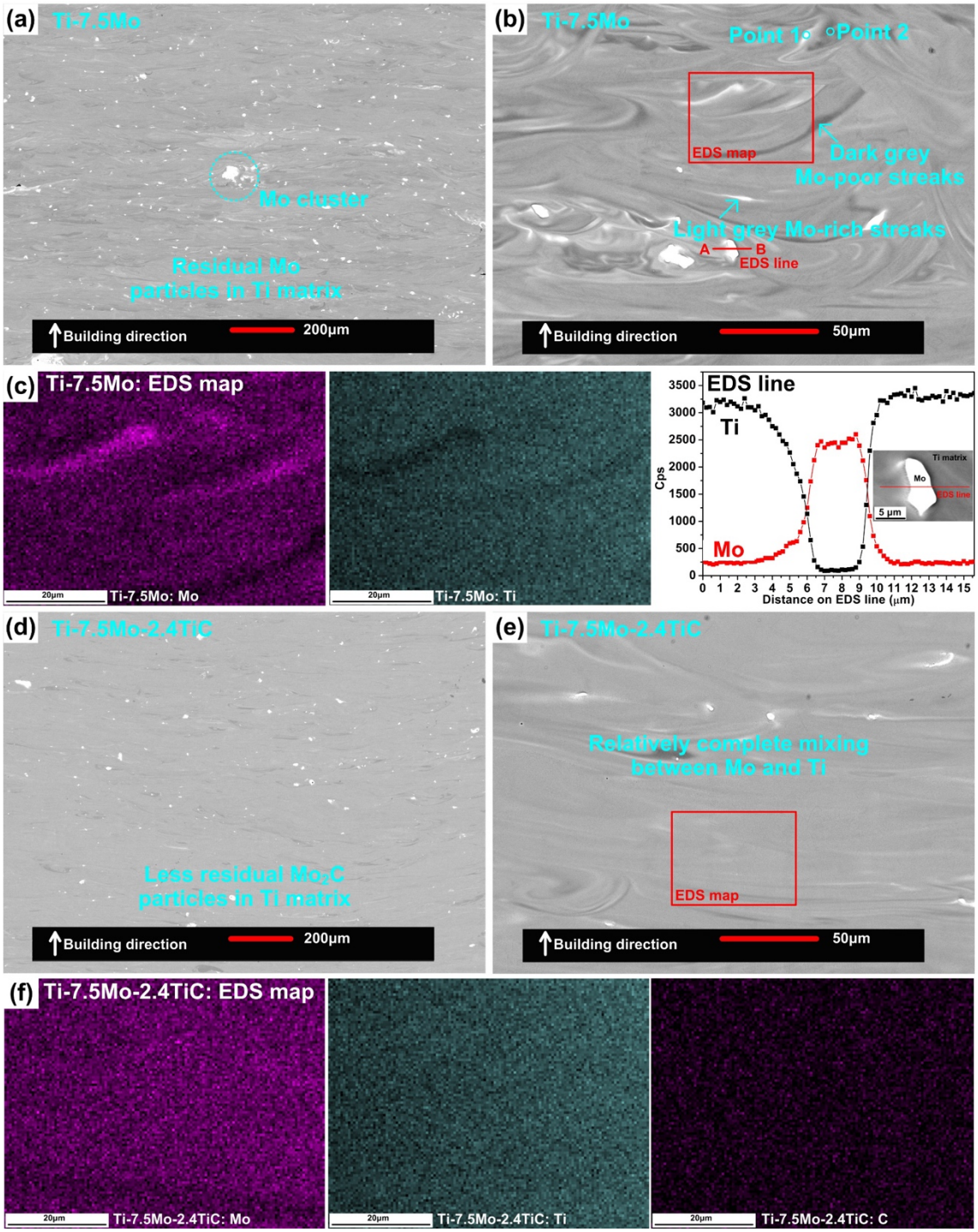

Fig. 4. BSE-SEM images and EDS analyses showing chemical homogeneity in SLM-fabricated (a-c) Ti-7.5Mo alloys and (d-f) in-situ Ti-7.5Mo-2.4TiC composites. The red rectangle and red line in (b) highlight the EDS map region and EDS line region shown in (c); the red rectangle in (e) highlights the EDS map region shown in (f).

3.2 Microstructural development within Ti-7.5Mo alloys and in-situ Ti-7.5Mo-2.4TiC composites

3.2.1 Phase identification

Body-centred cubic (bcc) β phase and hexagonal close-packed (hcp) α phase are detected in both Ti-7.5Mo alloys and in-situ Ti-7.5Mo-2.4TiC composites fabricated by SLM, as evidenced by XRD spectra (Fig. 5). As a result of 15% more β-stabiliser, Mo, introduced into the Ti matrix of the in-situ Ti-7.5Mo-2.4TiC composites than the Ti-7.5Mo alloys, the in-situ Ti-7.5Mo-2.4TiC composites show stronger β peaks and weaker α ones. Although α-stabilisers like O, N and C were also introduced to the material due to the chemical contamination from the raw powders, considering their very

low contents compared to Mo, Mo can dominate the β→α phase transformation in this work. As evaluated by the RIR method, the in-situ Ti-7.5Mo-2.4TiC composites have 68.1% β phase, increasing by 61.4% compared to the Ti-7.5Mo alloys (Table 2). The precipitated TiC in the in-situ Ti-7.5Mo-2.4TiC composites is confirmed by the 2θ peaks at 36.0º, 41.8º and 60.6º; weak peaks of Mo and Mo_2C phase are also identified, corresponding to the residual Mo or Mo_2C particles observed in the specimen (Fig. 4). Closer observation shows shifting of 2θ peaks of β phase to higher degrees in both Ti-7.5Mo alloys and in-situ Ti-7.5Mo-2.4TiC composites, compared with the standard 2θ values (PDF#89-4913), while the inter-planar spacing of β(110) declines (Fig. 5(b)). Differently, the in-situ Ti-7.5Mo-2.4TiC composites own more noticeable shifting of 2θ peaks of β phase, whose peak width becomes broadened at the same time, implying the formation of refined microstructures. In contrast, the 2θ peaks of α phase shift to lower degrees (PDF#89-3725) with an increased inter-planar spacing of α(101). The decline of the lattice constant of the β phase can be due to the lattice distortion mainly induced by the substitution of small-sized Mo (and C) in the Ti matrix during the non-equilibrium metallurgical processing ($Mo_{atom\text{-}radius}$= 0.136 nm vs $Ti_{atom\text{-}radius}$= 0.147 nm [37]). More Mo atoms dissolved into the in-situ Ti-7.5Mo-2.4TiC composites (7.06 wt% in in-situ Ti-7.5Mo-2.4TiC composites vs 6.14 wt% in Ti-7.5Mo alloys; Fig. 4) results in the significantly noticeable shrink of the lattice of β phase and the resultant shifting of Bragg reflection angles to higher degrees. While, the most plausible reason for the widened inter-planar spacing of α(101) can be ascribed to the different levels of residual stresses accumulated during the growth of α phase with various morphologies at different temperature ranges during the solidification of SLM [38, 39].

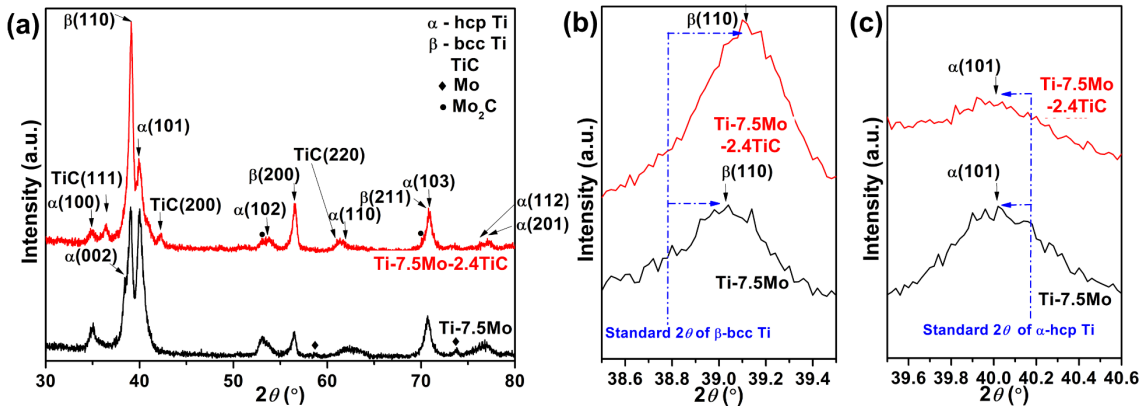

Fig. 5. XRD spectra of SLM-fabricated Ti-7.5Mo alloys and in-situ Ti-7.5Mo-2.4TiC composites obtained (a) over a wide range of 2θ (20º - 80º) and (b) in the vicinity of 2θ = 38.758º of β phase and (c) in the vicinity of 2θ = 40.177º of α phase.

Table 2. Quantitative XRD data revealing the shifting of 2θ peaks and variation of inter-planar spacing, and weight fractions of α and β phase in SLM-fabricated Ti-7.5Mo alloys and in-situ Ti-7.5Mo-2.4TiC composites.

Specimens	1st strong peak of β phase		1st strong peak of α phase		
	2θ (º)	$d_{(110)}$ (Å)	2θ (º)	$d_{(101)}$ (Å)	β phase (%)/ α phase (%)
Stanard	38.758	2.3214	40.177	2.2427	/
Ti-7.5Mo	39.04	2.3089	40.02	2.2546	42.2/ 57.8
Ti-7.5Mo-2.4TiC	39.10	2.3055	40.02	2.2547	68.1/ 31.9

3.2.2 Microstructural features

Figure 6 illustrates the microstructure of the Ti-7.5Mo alloys and in-situ Ti-7.5Mo-2.4TiC composites fabricated by SLM. On the macroscale, besides residual Mo particles, molten pools in the Ti-7.5Mo alloys were sketched by differently etched Mo-rich and Mo-poor streaks, showing average molten pool dimensions of around 102 μm (Width) × 42 μm (Depth) (Fig. 6(a)). Conversely, the SLM-fabricated in-situ Ti-7.5Mo-2.4TiC composites were etched relatively homogenously due to the relatively complete mixing between Mo and Ti (Fig. 4(d)), leaving a comparatively flat morphology. The average molten pool size of the in-situ Ti-7.5Mo-2.4TiC composites slightly grows to 105 μm (Width) × 44 μm (Depth) (Fig. 6(c)). Moreover, Fig. 6(a) and 6(c) both show columnar prior β grains, and the β columns in the in-situ Ti-7.5Mo-2.4TiC composites are typically 5-12 μm in diameter, which are thinner than 7-20 μm of the β grains in the Ti-7.5Mo alloys and also shorter in length. The compact β grains in the in-situ Ti-7.5Mo-2.4TiC composites induces a narrower β column spacing. In addition, the β grains grow epitaxially across molten pools, forming elongated ones along the building direction. Closer observation further illustrates a step-like growth of these β columns, highlighted by white arrows in Fig. 6(a). According to solidification theory, solutes are rejected to the front of the solid-liquid interface during the solidification of alloys, leading to a constitutional undercooling region. In this work, grains nucleate at the molten pool boundary where constitutional undercooling forms first and grow on the previously solidified but partially remelted β columns, leaving the continuous β columnar growth. While the step-like feature is due to the rearrangement of molten pools between two adjacent layers by periodically moving the laser scanning islands during the SLM (Fig. 1(c)).

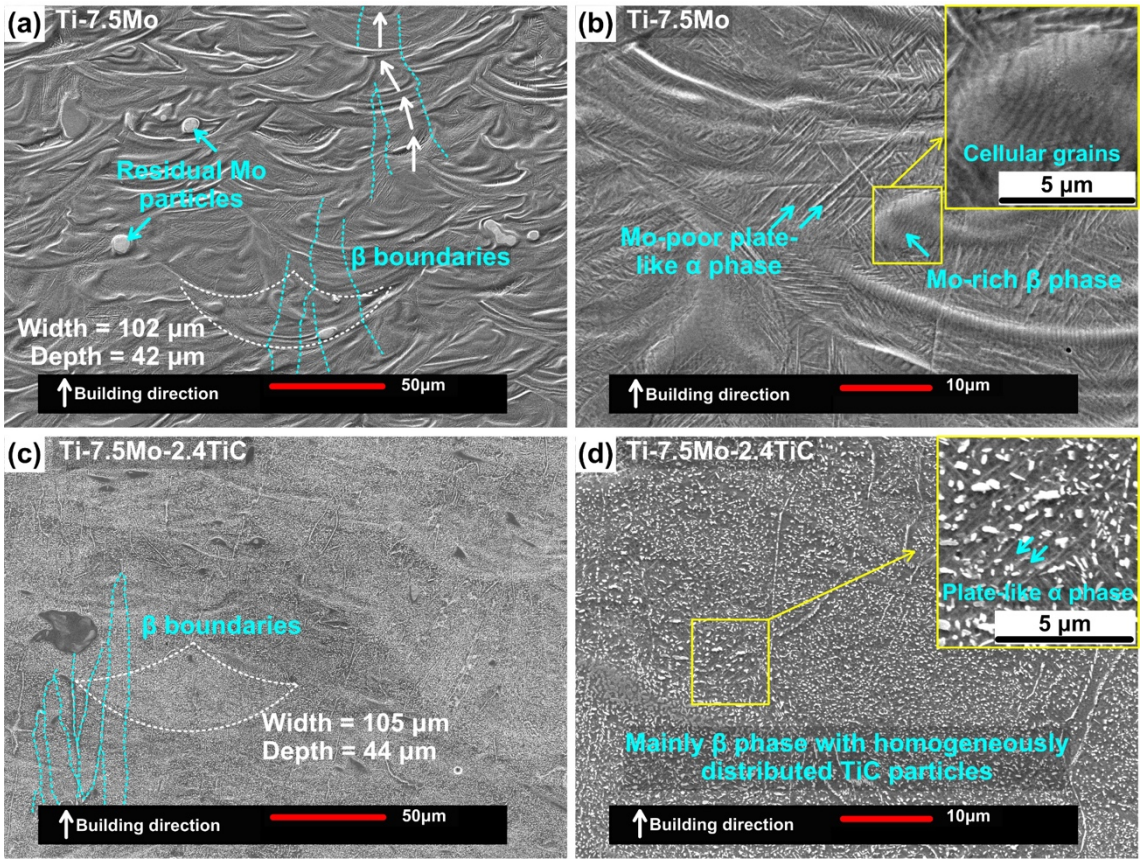

Fig. 6. SE-SEM images showing microstructural features in SLM-fabricated (a, b) Ti-7.5Mo alloys and (c, d) in-situ Ti-7.5Mo-2.4TiC composites.

According to the Mo-Ti binary phase diagram [40], Mo and β-Ti are infinitely miscible; however, the maximum Mo solubility in α-Ti is less than 1 wt%. Therefore, on the microscale, the Mo-rich region in the Ti-7.5Mo alloys with up to 20.62 wt% Mo tends to be β-Ti, which is in agreement with the phase response of casting Ti-Mo alloys with ≥ 15 wt% Mo [41]. Closer observation shows that the β-Ti consists of cellular substructures with an intercellular spacing of less than 400 nm. Such a cellular morphology was also reported in a Ti-6Al-4V+Mo system [42], Ti-Nb system [43] and Ti-Ta system [44] processed by SLM. While the Mo-poor region can be α-Ti, showing plate-like morphologies (Fig. 6(b)). As the result of higher Mo content in the Ti matrix, α-Ti is comparatively less visible in the in-situ Ti-7.5Mo-2.4TiC composites. Instead, homogeneously distributed precipitates are seen. EDS analysis reveals an atomic Ti/C ratio of approximately 1:1 within those precipitates, indicating the formation of TiC, which coincides with the XRD analysis. TiC particles form necklaces along the prior β grain boundaries and distribute across the grains. α-Ti plates can only be observed locally by closer observation, see the inset in Fig. 6(d). The less visible α-Ti plates, in turn, confirms the decline of the intensity of 2θ peaks corresponding to the α phase in the SLM-fabricated in-situ Ti-7.5Mo-2.4TiC composites (Fig. 5 and Table 2).

For CPRMMCs, it is well known that the size and shape of reinforcement particles and their distribution state within the metal matrix play a key role in determining the mechanical properties [23]. The morphology of TiC particles and their size distribution are illustrated in Fig. 7. The black-contrast TiC particles show to be well bonded with the Ti

matrix, as revealed by the BSE image before sample etching (Fig. 7(a)). The good interfacial bonding between the in-situ precipitated ceramics and the metal matrix is one of the remarkable advantages of the SLM-fabricated CPRMMCs via the in-situ synthesis mechanism, which benefits the smooth loading transferring and sharing across the interface and therefore enhances material strength [45]. Afterwards, the sample etching reveals that the TiC particles approximate an elongated spheroidal shape with various long and short diameters. The local edge of the TiC can be rough and even polygonal (Fig. 7(b)). By determining the particle size distribution from at least 200 exposed particles, it can be found that the elongated spheroidal TiC owns an average long diameter of 229.6 nm and an average short diameter of 80 nm with an aspect ratio (long/short diameter) of 2.71 (Fig. 7(c-e)).

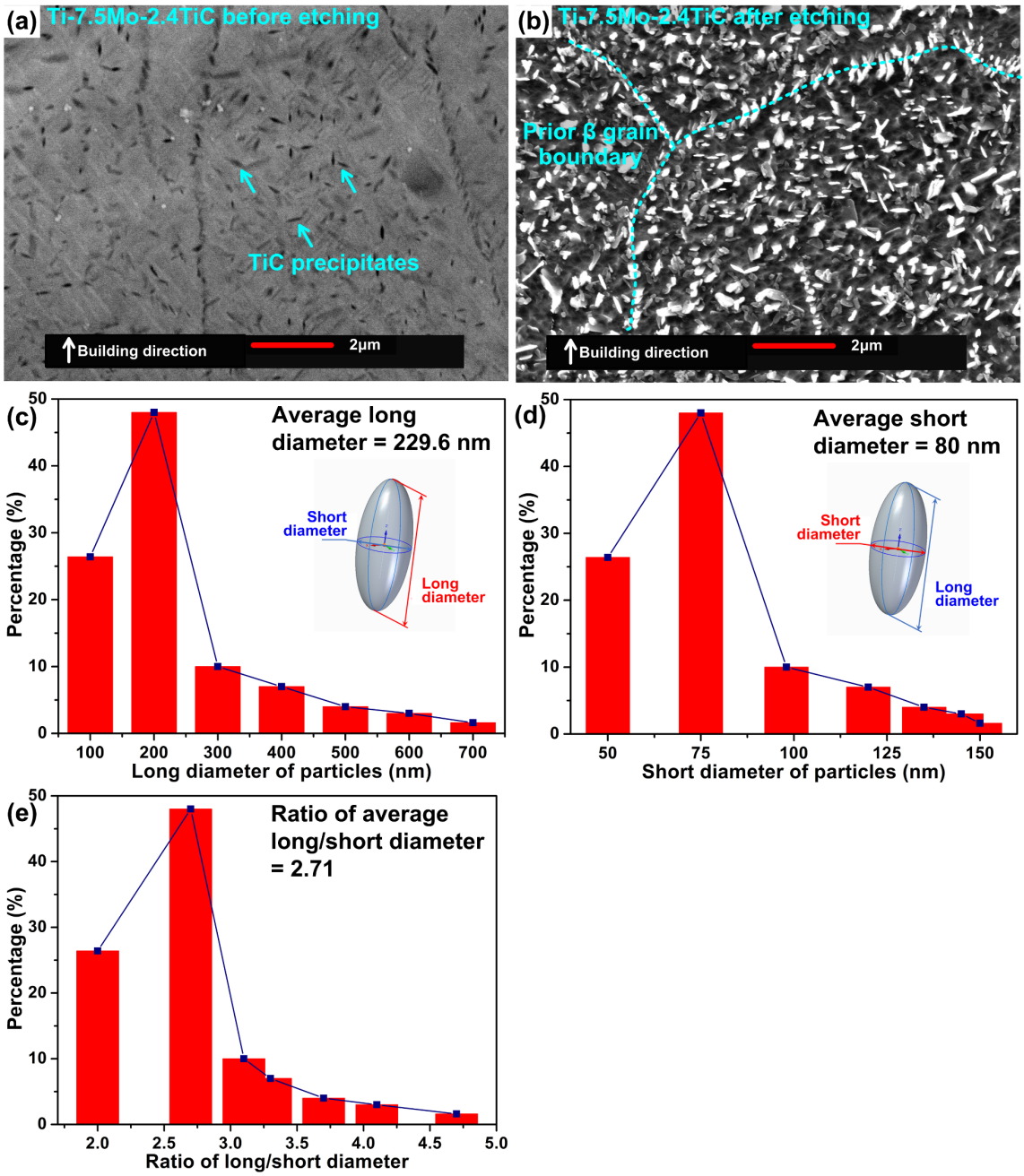

Fig. 7. (a-b) BSE/SE-SEM images showing the typical morphology of TiC particles in SLM-fabricated in-situ Ti-7.5Mo-2.4TiC composites and (c-e) their size distribution.

3.2.3 Thermal mechanisms behind microstructural development

The thermal behaviour within the molten pool during the SLM process plays a crucial role in determining the microstructural development and the resulting mechanical performance [46]. Numerical simulation has become a widely accepted method to quantitatively study the thermal mechanism behind microstructural development, given the challenge to measure the thermal data in real-time during the SLM under a super fast moved heat source (>1000 mm/s in this study), limited liquid lifetime within several milliseconds and extremely high cooling rate of up to 10^{6-7} K/s [34]. The transient temperature contour plots within the cross-section of the Ti-7.5Mo alloys and in-situ Ti-7.5Mo-2.4TiC composites during the SLM are demonstrated in Fig. 8. The red line, representing the melting temperature of Ti (1933 K), sketches a molten pool, showing the predicted molten pool dimensions of 97 μm (Width) × 40.5 μm (Depth) for the Ti-7.5Mo alloys and 101 μm (Width) × 42 μm (Depth) for the in-situ Ti-7.5Mo-2.4TiC composites. It is seen that a small error of less than 5.2% between the molten pool size predicted by numerical simulation (Fig. 8) and the size experimentally measured on the cross-section of the specimen (Fig. 6(a) and 6(c)) is achieved, to some degree verifying the accuracy and reliability of the numerical simulation model.

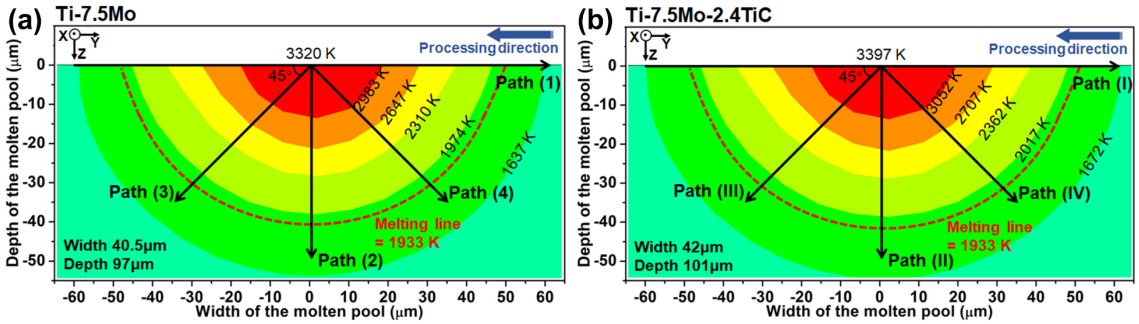

Fig. 8. Transient temperature contour plots of the molten pool of (a) Ti-7.5Mo alloys and (b) Ti-7.5Mo-2.4TiC composites during the SLM with paths assigned to monitor the temperature and temperature gradient.

Four typical orientations originating from the molten pool centre (Path (1-4) and Path (I-IV), Fig. 8) with a 45° intersection angle between the adjacent two ones were further monitored to study the spatial variation of the temperature gradient across the molten pool. The temperature distribution along Path (1-4) and Path (I-IV) are shown in Fig. 9, and the slope of the temperature curve indicates the temperature gradient. The mechanism behind the microstructural development of the Ti-7.5Mo alloys and Ti-7.5Mo-2.4TiC composites is concluded in Fig. 10. The relationship among primary Dendrite Arm Spacing (DAS, namely the β column spacing in this work) (d_1), growth rate (V_{GR}) and temperature gradient (G) [47]:

$$d_1 = \mathrm{K} V_{GR}^{-0.25} G^{-0.5} \quad (8)$$

where K is a material constant of the Ti-Mo matrix, shows that d_1 decreases proportionally with increasing V_{GR} or G. Figure 9 reveals that the maximum G both happens on the depth orientation of the molten pool (Path (2) and Path (II)). That explains the development of β grains along the building direction in both Ti-7.5Mo alloys and in-situ Ti-7.5Mo-2.4TiC composites prepared by SLM (Fig. 10). A higher G of 51.2 K/μm for the in-situ Ti-7.5Mo-2.4TiC composites

can be responsible for the more compact arrangement of β grains and the resulting smaller β column diameters (Fig. 6(c)) compared to the Ti-7.5Mo alloys, considering Equation (8). Furthermore, the extra precipitated TiC with higher thermal conductivity (23 W/(m·K) than Ti(-Mo) matrix (21.8 W/(m·K) within the in-situ Ti-7.5Mo-2.4TiC composites can make the heat dissipation faster from the molten pool to the solidified bulk, compared to Ti-7.5Mo alloys without TiC. A rapid cooling process would accelerate the solidification and terminate grain growth, forming fine microstructures. What's more, TiC particles can act as nucleation sites to accelerate heterogeneous nucleation (Fig. 10(b)), also benefiting the β grain refinement in the in-situ Ti-7.5Mo-2.4TiC composites. Furthermore, the pinning effect of the TiC at β grain boundaries, shown as a form of necklaces in Fig. 7(a), could restrict the grain growth during the solidification. Therefore, it is reasonable to consider that a higher temperature gradient and a more rapid cooling process, together with TiC precipitates, result in the shorter and thinner columnar β grains in the in-situ Ti-7.5Mo-2.4TiC composites.

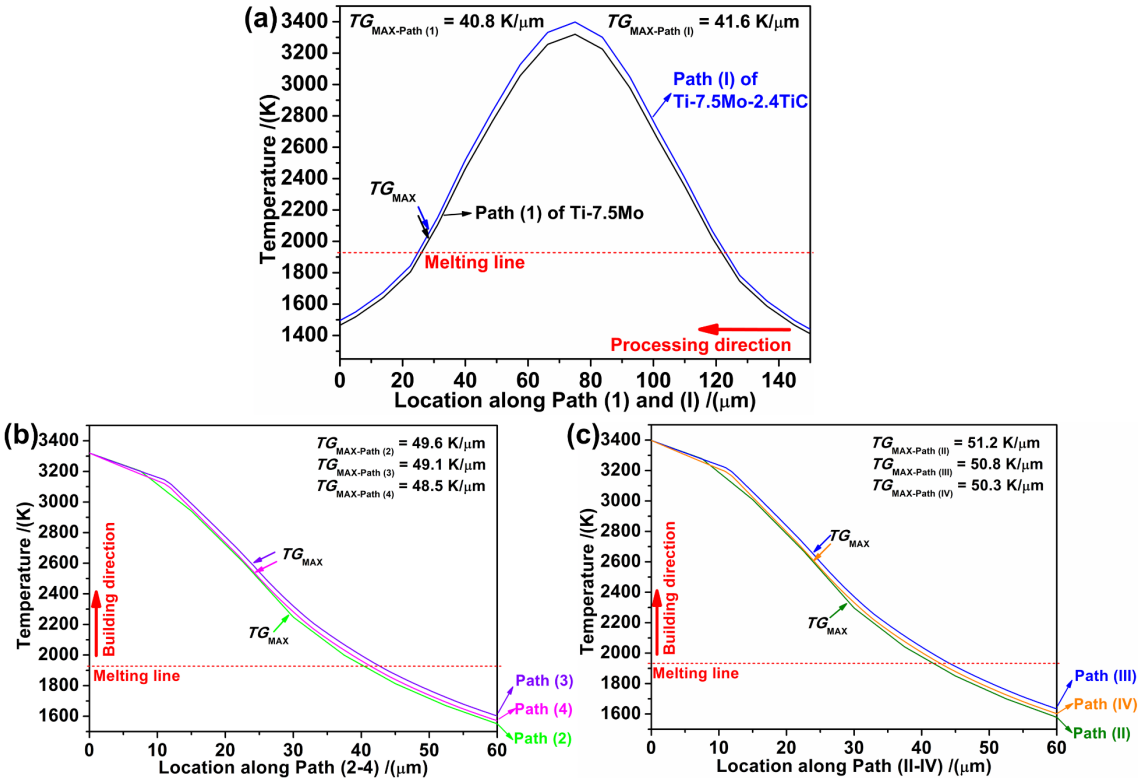

Fig. 9. Temperature distribution along typical orientations within the molten pool of Ti-7.5Mo alloys and in-situ Ti-7.5Mo-2.4TiC composites fabricated by SLM.

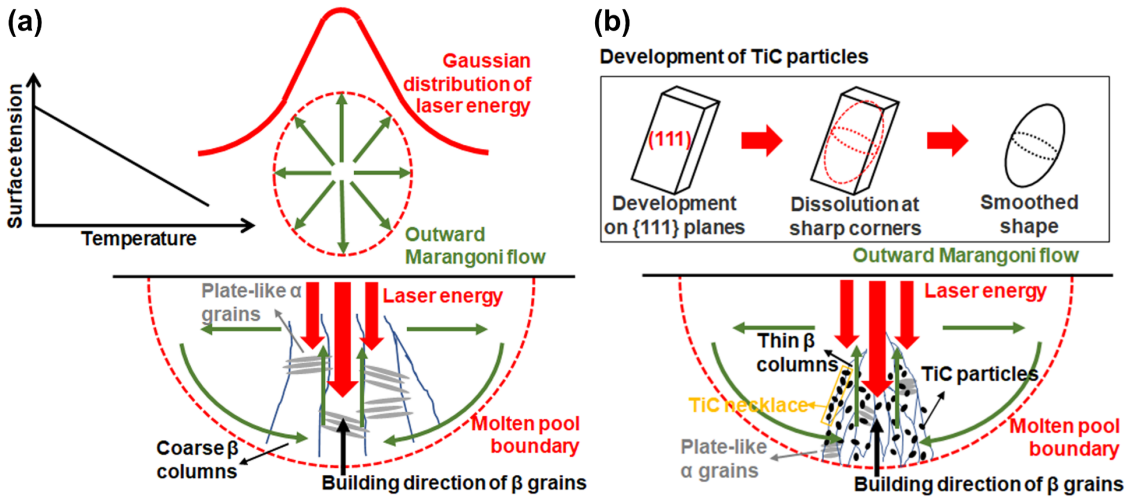

Fig. 10. Mechanisms behind the microstructural development of (a) Ti-7.5Mo alloys and (b) in-situ Ti-7.5Mo-2.4TiC composites fabricated by SLM.

Elongated spheroidal TiC particles in the in-situ Ti-7.5Mo-2.4TiC composites were precipitated (Fig. 7). In fact, TiC develops via a dissolution-precipitation mechanism by the heterogeneous nucleation of TiC nuclei and their subsequent grain growth [48]. As a NaCl-type faceted crystal, {111} planes of TiC own the highest surface atomic density, as well as the lowest surface energy. Therefore, TiC primarily precipitates and grows on the {111} planes, forming lamellar structures with sharp corners [49]. Due to a higher specific surface area, these sharp corners can absorb more laser energy, causing a higher temperature and a higher dissolution rate within the metal liquid. Consequently, fine lamellar TiC is finally smoothened and approximates an elongated spheroidal shape (Fig. 10(b)).

Regarding the TiC distribution state within the matrix of in-situ Ti-7.5Mo-2.4TiC composites, firstly, although precipitated particles tend to segregate at grain boundaries due to the pushing effect by the solidification front of metal liquid, as revealed by previous studies [50], TiC particles in this study can be retained across the Ti matrix, which could be due to the capture effect by the solidification front. The Stokes' formula [51]:

$$v_P = 2/9 \times [g r_P^2(\rho_l - \rho_P)]/\eta \quad (9)$$

where v_P is the particle velocity, g is gravity acceleration, r_P is the particle radius, η is the viscosity of the metal liquid, and ρ_l and ρ_P are the density of the metal liquid and the particle, respectively, indicates that TiC particles can be captured by the solidification front and kept inside the Ti cells, when lowering the particle velocity slower than the solidification rate by decreasing the TiC particle size to a certain level (below 229.6 nm in this work). Secondly, the homogeneous distribution of the TiC particles across the metal matrix can also be attributed to Marangoni flows, as suggested by Gu et al. [52]. As shown in Fig. 10, the laser energy with a Gaussian distribution suggests higher energy intensity at the molten pool centre than that at the periphery, causing higher temperature at the molten pool centre. The surface tension of the metal liquid owns a negative correlation with the temperature. Thus, the spatial temperature variation and resultant surface tension difference can cause the liquid within the molten pool to be drawn along the surface from the region having low surface tension to the region having high surface tension, forming outward

Marangoni convections. The thermal capillary force driven by the Marangoni flow contributes to the rearrangement of TiC particles. Finally, Brownian movement driven by thermal energy, E_b, is also helpful to the homogeneous distribution of TiC. The E_b can be evaluated by [53]:

$$E_b = \sigma T \tag{10}$$

where T is absolute temperature, and σ is Boltzman constant. The high temperature of the metal liquid in the in-situ Ti-7.5Mo-2.4TiC composites (up to 3397 K, Fig. 8(b)) can lead to a high E_b and strong Brownian movement, benefiting the dispersion of the TiC particles. Therefore, it is reasonable to expect the homogeneous distribution of the TiC particles in the SLM-fabricated in-situ Ti-7.5Mo-2.4TiC composites considering the capture effect by the solidification front, Marangoni flows, and strong Brownian movement.

3.3 Mechanical and wear performance of Ti-7.5Mo alloys and in-situ Ti-7.5Mo-2.4TiC composites

3.3.1 Mechanical properties

Compressive tests show less susceptibility than tensile tests to minor processing defects that can cause premature failure. Therefore, compressive test results can exhibit the intrinsic property of the material. Figure 11 shows the engineering compressive stress-strain curve of the SLM-fabricated Ti-7.5Mo alloys and in-situ Ti-7.5Mo-2.4TiC composites and their quantitative mechanical properties with a comparison to other Ti-Mo materials from SLM or traditional routes. The stress increases rapidly initially and continues to grow after the yield point but at an increasingly lower rate (Fig. 11(a)). Then, the stress drops suddenly until final failure, leaving a 33% lower ultimate strain of the in-situ Ti-7.5Mo-2.4TiC composites (A, 5.4%) than that of the Ti-7.5Mo alloys (A, 8.1%). However, as summarised in Fig. 11(b), the yield strength (YS, 980.1 ± 29.8 MPa) and ultimate compressive strength (UCS, 1561.4 ± 39 MPa), as well as the microhardness (H, 447 ± 9 HV), of the in-situ Ti-7.5Mo-2.4TiC composites are well improved by up to 12.1% compared to the Ti-7.5Mo alloys (YS, 874.5 ± 17.6 MPa; UCS, 1463.2 ± 35 MPa; H, 404 ± 12 HV). The yield strength and ultimate strength of the Ti-7.5Mo alloys in this work show comparable and even superior in some cases to those of the Ti-7.5Mo alloys from SLM and traditional routes; the ultimate strength of the in-situ Ti-7.5Mo-2.4TiC composites in this work is comparable to those in similar SLM practices elsewhere (Fig. 11(b)). The high yield strength benefits patients by enhancing the capacity of the biomaterial against permanent shape change. The elastic modulus (E) of the Ti-7.5Mo alloys in this work (63.5 ± 1.3 GPa) is quite close to those of the Ti-7.5Mo counterparts prepared elsewhere, such as the casted and solution treated Ti-7.5Mo alloys consisting of fine, acicular martensitic α" phase (70 GPa [54]). However, the in-situ Ti-7.5Mo-2.4TiC composites improve its E to 91.9 ± 2 GPa, increasing by 44.7% compared with the E value of the SLM-fabricated Ti-7.5Mo alloys. Nevertheless, the E of the SLM-fabricated Ti-Mo alloys and composites in this work is still lower than that of traditional Ti-6Al-4V (about 110 GPa [1]), hopefully lowering the possibility to occur stress shielding effect clinically.

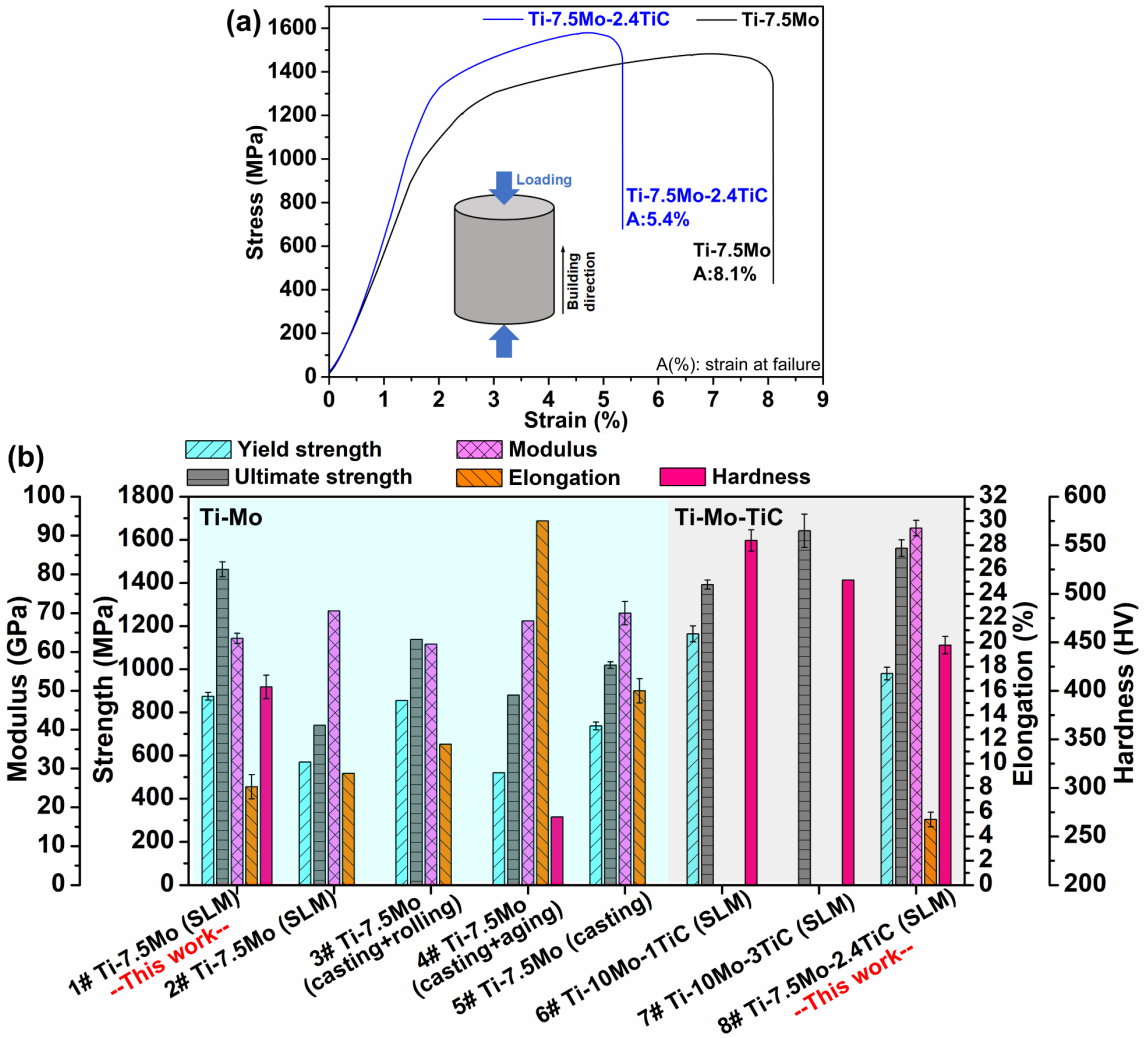

Fig. 11. (a) Engineering compressive stress-strain curves of SLM-fabricated Ti-7.5Mo alloys and in-situ Ti-7.5Mo-2.4TiC composites in as-built condition, and (b) their mechanical properties with a comparison to other Ti-Mo counterparts: 1# Ti-7.5Mo alloys in this work, 2# Ti-7.5Mo alloys by SLM elsewhere [26], 3# Ti-7.5Mo alloys by casting+rolling [55], 4# Ti-7.5Mo alloys by casting+aging [56], 5# Ti-7.5Mo alloys by casting [54], 6# in-situ Ti-10Mo-1TiC composites by SLM [17], 7# in -situ Ti-10Mo-3TiC composites by SLM [57], and 8# in-situ Ti-7.5Mo-2.4TiC composites in this work.

The enhancement of the yield/ultimate strength and hardness of the specimens fabricated by SLM is mainly ascribed to the refinement of Ti grains (Hall-Petch relationship) under a rapid solidification process, as widely revealed in SLM of titanium elsewhere [26], and, additionally, the reinforcement effect caused by the precipitated hard TiC for the in-situ Ti-7.5Mo-2.4TiC composites. Through the pinning effects from the TiC particles, the movement of dislocations and cell boundaries can be restricted, contributing to strength and hardness while lowering ductility. Also, Orowan strengthening can occur due to an artificial reduction in spacing between the particle reinforcements after the creation of Orowan loops, increasing the initial work hardening rate in CPRMMCs and contributing to strength [58]. Furthermore, the in-situ TiC particles having a strong bonding with the Ti matrix, shown in Fig. 7(a), can effectively share the load during the deformation, further improving the total strength of the composites [45]. Besides, it should also be noted that, although the chamber atmosphere has been carefully controlled during SLM to avoid the O and N contamination from the outside atmosphere, O and N can still be introduced into the alloys/composites due to the impurity of the raw powders, and strengthen the material to some degree via a solid-solution strengthening mechanism

while sacrificing the ductility [30]. EDS point scan confirms < 0.14 wt% of O and < 0.05 wt% of N on the polished specimen surface, while the factual content of these elements inside the material could be lower than the measured values considering the O and N attachment on the specimen surface during specimen polishing in air atmosphere.

The elastic modulus of Ti-based alloys shows high sensitivity to internal phase/crystal structures [11]. There are mainly five types of phases in the rapidly cooled Ti-based alloys: α, β, α', α" and ω. The β phase owns the lowest elastic modulus, and the ω phase owns the highest one [11], and α", α', and α phase have in-between moduli. Therefore, the mixed α and β phase can explain the lower modulus of the Ti-7.5Mo alloys by SLM than the traditional SLM-fabricated Ti-6Al-4V mainly consisting of α' and α phase [1]. The higher elastic modulus of the in-situ Ti-7.5Mo-2.4TiC composites although with 61.4% more low-modulus β phase than the Ti-7.5Mo alloys in this work (Table 2), can be ascribed to the precipitation of rigid TiC particles. The elastic modulus of a composite (E_C) can be estimated by a Halpin-Tsai model [59]:

$$E_C = E_M [(1 + 2smV_P)/(1 - mV_P)] \quad (11)$$

$$m = (E_P/E_M - 1)/(E_P/E_M + 2s) \quad (12)$$

where E_P and E_M are the elastic modulus of the ceramic particle and the metal matrix, respectively. s is the particles' aspect ratio (s = 2.71 in this work, Fig. 7), and V_P is the volume fraction of the ceramic particles. Considering the higher elastic modulus of TiC (450 GPa) compared to the Ti matrix, m is larger than zero. Thus, according to equation (11), E_C can be larger than E_M, since $[(1 + 2smV_P)/(1 - mV_P)]$ is larger than one due to a positive m and V_P.

As to further understand the fracture mechanism behind the Ti-Mo biomaterials, Fig. 12 illustrates the fractographs of the SLM-fabricated Ti-7.5Mo alloys and in-situ Ti-7.5Mo-2.4TiC composites. Generally, the fracture surface both shows a mixture of rough zones consisting of dimples and smooth shear zones (Fig. 12(a) and 12(c)). Fractographic analysis reveals that the specimen failure is mainly due to the shear fracture and axial splitting, causing a step-like fracture (Fig. 12(b) and 12(d)). As discussed above, the TiC particles leave higher material strength and hardness but lower ductility. The relatively poor ductility causes the microcracks and small-sized and shallow dimples (see the inset in Fig. 12(c)) in the in-situ Ti-7.5Mo-2.4TiC composites. During the deformation, the resistance to dislocation motion gradually increases as the increasing number of dislocations decreases the spacing between dislocations, and higher stress is necessary to deform the material. For the SLM-fabricated Ti-7.5Mo alloys, the α+β phase can accommodate the deformation until reaching the UCS of 1463.2 ± 35 MPa; while for the in-situ Ti-7.5Mo-2.4TiC composites, the TiC particles further enhance the resistance of dislocation motion during the deformation, causing a higher UCS of 1561.4 ± 39 MPa.

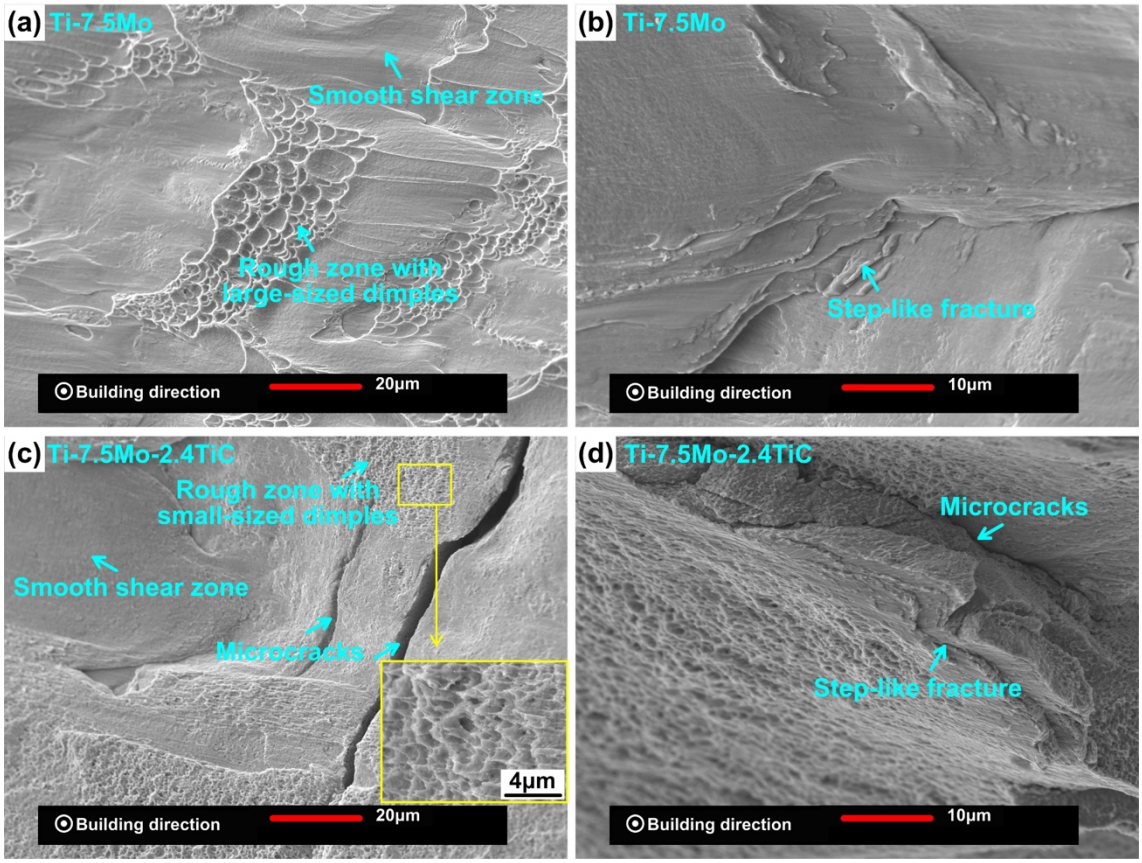

Fig. 12. SE-SEM compressive fractographs of the SLM-fabricated (a, b) Ti-7.5Mo alloys and (c, d) in-situ Ti-7.5Mo-2.4TiC composites.

3.3.2 Wear properties

Figure 13 records the wear properties of the Ti-7.5Mo alloys and the in-situ Ti-7.5Mo-2.4TiC composites fabricated by SLM. Figure 13(a) shows severe curve fluctuation at the initial stage. As the sliding process continues, the curve fluctuation is alleviated, and the ceramic ball lowers gradually, indicating the removal of material from the specimen surface. A smaller decrement of Z position (ΔZ) for the in-situ Ti-7.5Mo-2.4TiC composites suggests a shallower wear scar (depth of 29.1 ± 1.0 μm) than the Ti-7.5Mo alloys (depth of 38.4 ± 1.2 μm). Meanwhile, a narrower wear scar width was measured on the in-situ Ti-7.5Mo-2.4TiC composites (877 ± 15 μm of in-situ Ti-7.5Mo-2.4TiC composites vs 923 ± 17 μm of Ti-7.5Mo alloys) (Fig. 13(b)). According to Equation (7), the SLM-fabricated in-situ Ti-7.5Mo-2.4TiC composites produce a much lower material wear rate (6.98 $\times 10^{-4}$ $mm^3N^{-1}m^{-1}$) than the Ti-7.5Mo alloys (11.03 $\times 10^{-4}$ $mm^3N^{-1}m^{-1}$), decreasing by 36%.

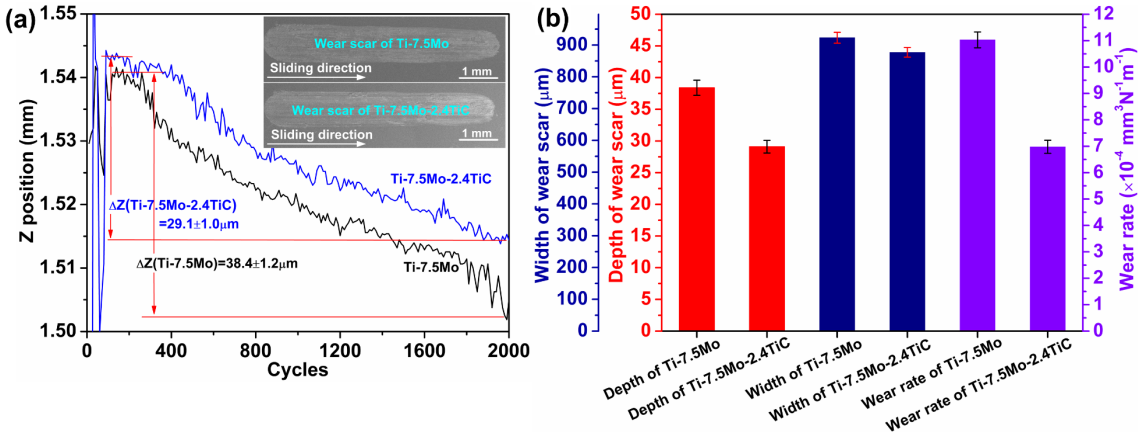

Fig. 13. (a) Record of lowest ceramic ball positions of ceramic balls during 2000 wear cycles and (b) wear properties including wear scar depth, wear scar width and wear rate of SLM-fabricated Ti-7.5Mo alloys and in-situ Ti-7.5Mo-2.4TiC composites.

As to understand the different wear mechanisms behind the material removal, the worn surface of the SLM-fabricated Ti-7.5Mo alloys and in-situ Ti-7.5Mo-2.4TiC composites are shown in Fig. 14. A large area of material spallation/delamination can be observed in the Ti-7.5Mo alloys with wear debris clusters, leading to more material loss and also the Z-position curve fluctuation deed at the initial stage (Fig. 14(a)). High magnification shows wide plowing grooves with a smooth surface under wear debris bulks, presenting the wear mechanism is dominated by severe abrasive wear (Fig. 14(b)). For the in-situ Ti-7.5Mo-2.4TiC composites, the overall worn surface is comparatively flat with fine wear debris above (Fig. 14(c)). Closer observation shows narrow plowing grooves, suggesting an alleviated abrasive wear mechanism. In addition, partially exposed TiC particles are seen on the worn surface, making the surface of the plowing grooves seem to be rough. The high-magnification inset in Fig. 14(d) further reveals that these exposed TiC particles are still well bonded with the Ti matrix, confirming the reliable role the in-situ precipitated TiC played in sharing the loading during the wear cycles, as mentioned above.

The wear behaviour and underlying mechanisms are mainly determined by the microstructure and the resulting microhardness of the material, as concluded in Fig. 15. During the wear test, the comparatively soft Ti-7.5Mo alloys (404 ± 19 HV of Ti-7.5Mo alloys vs 447 ± 9 HV of in-situ Ti-7.5Mo-2.4TiC composites) can be removed relatively easily under the pressure from the ceramic counterpart (Fig. 15(a)), causing material delamination and spallation (Fig. 14(a)) and a resultant higher wear rate (11.03 $\times 10^{-4}$ $mm^3N^{-1}m^{-1}$, Fig. 13(b)). The large-sized debris bulks and clusters can act as abrasive particles in the following sliding process, leading to the wide plowing grooves on the worn surface (Fig. 14(b)). Although more ductile and soft β phase is retained in the in-situ Ti-7.5Mo-2.4TiC composites (Table 2), the uniformly precipitated TiC particles can effectively share the high pressure from the ceramic ball, as evidenced by the well-bonded TiC particles with the Ti matrix after 2000 wear cycles (Fig. 14(d)), and thereby slow down the material loss and form fine wear debris. That contributes to the narrower and shallower wear scar and lowers the wear rate (6.98 $\times 10^{-4}$ $mm^3N^{-1}m^{-1}$). The homogeneously precipitated hard TiC particles in the worn surface also contribute to a stable sliding process (Fig. 15(b)), which can explain the flat worn surface in the SLM-fabricated in-situ Ti-7.5Mo-

2.4TiC composites (Fig. 14 (c)). With the decrease of the wear debris (acting as abrasive particles in the following sliding process) in size, the plowing grooves can be narrowed (14(d)).

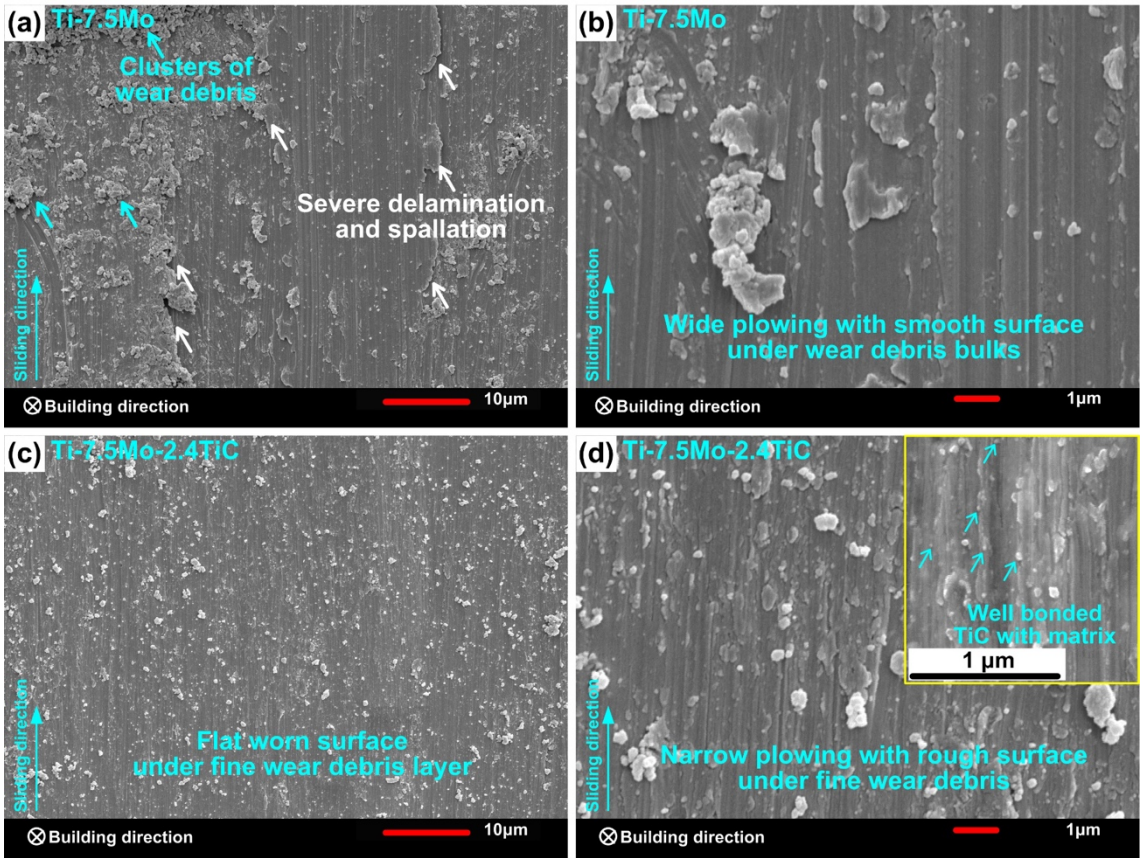

Fig. 14. SE-SEM images showing worn surface morphologies on (a, b) Ti-7.5Mo alloys and (c, d) in-situ Ti-7.5Mo-2.4TiC composites fabricated by SLM. The inset in (d) illustrates well bonded TiC particles with the Ti matrix.

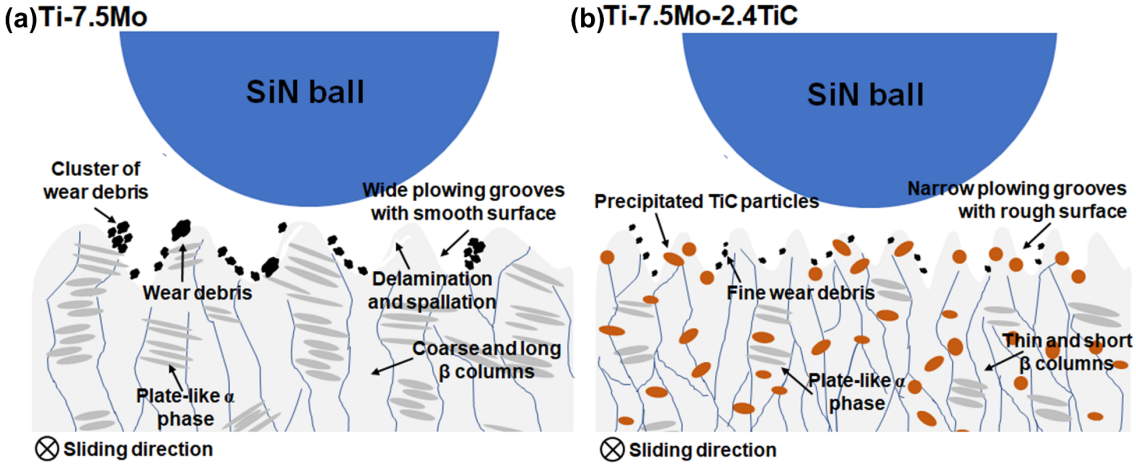

Fig. 15. Schematic showing the different wear mechanisms of (a) Ti-7.5Mo composites and (b) in-situ Ti-7.5Mo-2.4TiC composites fabricated by SLM.

4. Conclusions

Ti-7.5Mo alloys and in-situ Ti-7.5Mo-2.4TiC composites were prepared successfully by SLM starting from Ti/Mo and Ti/Mo_2C powder mixture, respectively. A comparative study on microstructure, mechanical and wear performance, and thermal mechanisms were explored to understand the different synthesis mechanisms of Ti-Mo biomaterials by SLM. The main conclusion can be drawn into:

(1) Residual unmolten or partially molten Mo or Mo_2C particles in the Ti matrix can still be seen in the SLM-fabricated parts. However, less Mo_2C is remained in the in-situ Ti-7.5Mo-2.4TiC composites due to a smaller total volume of Mo_2C provided initially and the in-situ Ti/Mo_2C exothermic reaction contributing to Mo diffusion. As a result, 15% higher Mo content (7.06 wt% Mo in in-situ Ti-7.5Mo-2.4TiC composites vs 6.14 wt% Mo in Ti-7.5Mo alloys) is achieved in the Ti matrix of the in-situ Ti-7.5Mo-2.4TiC composites, obtaining a comparatively homogeneous chemical distribution.

(2) Ti-7.5Mo alloys fabricated by SLM present a conchoidal two-phase α+β structure consisting of coarse and long columnar β grains and plate-like α grains due to the inhomogeneous chemical composition and stability. While in-situ Ti-7.5Mo-2.4TiC composites produce a comparatively homogeneous chemical distribution and develop more β phase (68.1%), increasing by 61.4% compared to the Ti-7.5Mo alloys. The internal columnar β grains in the in-situ Ti-7.5Mo-2.4TiC composites also show thinner and shorter. Thermal mechanisms reveal that a higher temperature gradient, a more rapid cooling process and the homogeneous precipitation of TiC particles lead to the thinner and shorter β columns in the in-situ Ti-7.5Mo-2.4TiC composites.

(3) SLM-fabricated in-situ Ti-7.5Mo-2.4TiC composites produce higher yield strength (YS, 980.1 ± 29.8 MPa) and ultimate compressive strength (UCS, 1561.4 ± 39 MPa) than Ti-7.5Mo alloys (YS, 874.5 ± 17.6 MPa; UCS, 1463.2 ± 35 MPa) with a strength increment of up to 12.1%. The mechanical property improvement of the in-situ Ti-7.5Mo-2.4TiC composites can be due to the grain refinement, pinning effect by fine TiC, Orowan strengthening and load sharing mechanism. However, the elastic modulus of the in-situ Ti-7.5Mo-2.4TiC composites (91.9 ± 2 GPa) is also improved by 44.7% than the value of SLM-fabricated Ti-7.5Mo alloys (63.5 ± 1.3 GPa). Results reveal that TiC and its aspect ratio of 2.71 are responsible for such modulus increment of the in-situ Ti-7.5Mo-2.4TiC composites.

(4) SLM-fabricated in-situ Ti-7.5Mo-2.4TiC composites present a much lower material wear rate (6.98×10^{-4} $mm^3N^{-1}m^{-1}$) with an alleviated abrasive wear mechanism, compared to Ti-7.5Mo alloys (11.03×10^{-4} $mm^3N^{-1}m^{-1}$), decreasing by 36%. That is mainly owing to the uniformly distributed TiC particles to share the loading.

(5) Although with higher modulus than the Ti-7.5Mo alloys, the SLM-fabricated in-situ Ti-7.5Mo-2.4TiC composites can expect to provide good biomedical application potential in cases where combined good strength and wear resistance are required.

Acknowledgement

The author, Qimin Shi, gratefully acknowledges the financial support from the China Scholarship Council (No. 201806830109), and the technical assistance from technician Mr Jo Van Kriekingen in the Department of Mechanical Engineering, KU Leuven, and technicians Ms Christel Butnaru, Mr Tom Van der Donck, Mr Bart Pelgrims, and Mr

Louis Depre in the Department of Materials Engineering, KU Leuven. Mr Qimin Shi also greatly appreciates the assistance from Dr Xiao Zhao, University of Southampton, UK, in the SLM experiments.

References

[1] L.-C. Zhang, H. Attar, Adv. Eng. Mater. 18 (2016) 463-475.
[2] A. Nouri, A. Rohani Shirvan, Y. Li, C. Wen, J. Mater. Sci. Technol. 94 (2021) 196-215.
[3] D. Ren, S. Li, H. Wang, W. Hou, Y. Hao, W. Jin, R. Yang, R.D.K. Misra, L.E. Murr, J. Mater. Sci. Technol. 35 (2019) 285-294.
[4] C. Cai, X. Wu, W. Liu, W. Zhu, H. Chen, J.C.D. Qiu, C.-N. Sun, J. Liu, Q. Wei, Y. Shi, J. Mater. Sci. Technol. 57 (2020) 51-64.
[5] J.E. Bechtold, Orthop. Clin. North Am. 17 (1986) 605-612.
[6] N. De Meurechy, A. Braem, M.Y. Mommaerts, Int. J. Oral Maxillofac. Surg. 47 (2018) 518-533.
[7] B. Mjöberg, E. Hellquist, H. Mallmin, U. Lindh, Acta Orthop. Scand. 68 (1997) 511-514.
[8] I. Zwolak, Toxicol. Mech. Methods 24 (2014) 1-12.
[9] N. Kang, X. Lin, M.E. Mansori, Q.Z. Wang, J.L. Lu, C. Coddet, W.D. Huang, Addit. Manuf. 31 (2020) 100911.
[10] A. Almeida, D. Gupta, C. Loable, R. Vilar, Mater. Sci. Eng. C. 32 (2012) 1190-1195.
[11] W.-d. Zhang, Y. Liu, H. Wu, M. Song, T.-y. Zhang, X.-d. Lan, T.-h. Yao, Mater. Charact. 106 (2015) 302-307.
[12] W. Xu, M. Chen, X. Lu, D.-w. Zhang, H.-p. Singh, Y. Jian-shu, Y. Pan, X.-h. Qu, C.-z. Liu, Corros. Sci. 168 (2020) 108557.
[13] N.T.C. Oliveira, A.C. Guastaldi, Acta Biomater. 5 (2009) 399-405.
[14] W.F. Ho, C.P. Ju, J.H. Chern Lin, Biomaterials 20 (1999) 2115-2122.
[15] N. Li, S. Huang, G. Zhang, R. Qin, W. Liu, H. Xiong, G. Shi, J. Blackburn, J. Mater. Sci. Technol. 35 (2019) 242-269.
[16] J. Vishnu, G. Manivasagam, J. Bio. Tribo. Corros. 7 (2021) 32.
[17] B. Vrancken, S. Dadbakhsh, R. Mertens, K. Vanmeensel, J. Vleugels, S. Yang, J.-P. Kruth, CIRP Annals 68 (2019) 221-224.
[18] M.H. Mosallanejad, B. Niroumand, A. Aversa, A. Saboori, J. Alloys Compd. 872 (2021) 159567.
[19] R. Duan, S. Li, B. Cai, W. Zhu, F. Ren, M.M. Attallah, Addit. Manuf. 37 (2021) 101708.
[20] Q. Shi, R. Mertens, S. Dadbakhsh, G. Li, S. Yang, J. Mater. Process. Technol. 299 (2022) 117357.
[21] P. Fischer, V. Romano, H.P. Weber, N.P. Karapatis, E. Boillat, R. Glardon, Acta Mater. 51 (2003) 1651-1662.
[22] Y.B. Liu, Y. Liu, H.P. Tang, B. Wang, B. Liu, J. Mater. Sci. 46 (2011) 902-909.
[23] S.C. Tjong, Adv. Eng. Mater. 9 (2007) 639-652.
[24] C. Han, R. Babicheva, J.D.Q. Chua, U. Ramamurty, S.B. Tor, C.-N. Sun, K. Zhou, Addit. Manuf. 36 (2020) 101466.
[25] N. Kang, X. Lin, C. Coddet, X. Wen, W. Huang, Mater. Lett. 267 (2020) 127544.
[26] N. Kang, Y. Li, X. Lin, E. Feng, W. Huang, J. Alloys Compd. 771 (2019) 877-884.
[27] H. Attar, K.G. Prashanth, L.-C. Zhang, M. Calin, I.V. Okulov, S. Scudino, C. Yang, J. Eckert, J. Mater. Sci. Technol. 31 (2015) 1001-1005.
[28] K. Lin, Y. Fang, D. Gu, Q. Ge, J. Zhuang, L. Xi, Advanced Powder Technology 32 (2021) 1426-1437.
[29] X. Ji, S. Emura, T. Liu, K. Suzuta, X. Min, K. Tsuchiya, J. Alloys Compd. 737 (2018) 221-229.
[30] T.-W. Na, W.R. Kim, S.-M. Yang, O. Kwon, J.M. Park, G.-H. Kim, K.-H. Jung, C.-W. Lee, H.-K. Park, H.G. Kim, Mater. Charact. 143 (2018) 110-117.
[31] J. Geng, Z. Zhu, Y. Ni, H. Li, F. Cheng, F. Li, J. Chen, Nano Res. (2021).
[32] Q. Shi, D. Gu, M. Xia, S. Cao, T. Rong, Opt. Laser. Technol. 84 (2016) 9-22.
[33] D. Gu, Q. Shi, K. Lin, L. Xi, Addit. Manuf. 22 (2018) 265-278.
[34] Y. Li, D. Gu, Addit. Manuf. 1-4 (2014) 99-109.
[35] K.H. Leitz, P. Singer, A. Plankensteiner, B. Tabernig, H. Kestler, L.S. Sigl, Metal Powder Report 72 (2017) 331-338.
[36] J.P. Kruth, X. Wang, T. Laoui, L. Froyen, Assembly Autom. 23 (2003) 357-371.
[37] S.H. Koutzaki, J.E. Krzanowski, J.J. Nainaparampil, Metall. Mater. Trans. A 33 (2002) 1579-1588.
[38] S. Malinov, P. Markovsky, W. Sha, Z. Guo, J. Alloys Compd. 314 (2001) 181-192.

[39] S. Malinov, W. Sha, Z. Guo, C.C. Tang, A.E. Long, Mater. Charact. 48 (2002) 279-295.
[40] D. Bandyopadhyay, B. Haldar, R.C. Sharma, N. Chakraborti, J. Phase Equilib. 20 (1999) 332-336.
[41] X. Zhao, M. Niinomi, M. Nakai, J. Hieda, Acta Biomater. 8 (2012) 1990-1997.
[42] B. Vrancken, L. Thijs, J.P. Kruth, J. Van Humbeeck, Acta Mater. 68 (2014) 150-158.
[43] D. Zhao, C. Han, J. Li, J. Liu, Q. Wei, Mater. Sci. Eng. C. 111 (2020) 110784.
[44] D. Zhao, C. Han, Y. Li, J. Li, K. Zhou, Q. Wei, J. Liu, Y. Shi, J. Alloys Compd. 804 (2019) 288-298.
[45] S. Dadbakhsh, R. Mertens, L. Hao, J. Van Humbeeck, J.-P. Kruth, Adv. Eng. Mater. 21 (2019) 1801244.
[46] Q.M. Shi, D.D. Gu, K.J. Lin, W.H. Chen, M.J. Xia, D.H. Dai, J. Manuf. Sci. Eng. 140 (2018) 111019.
[47] W. Kurz, D.J. Fisher, Acta Metall. 29 (1981) 11-20.
[48] G. Liu, K. Chen, H. Zhou, J. Guo, K. Ren, J.M.F. Ferreira, Mater. Lett. 61 (2007) 779-784.
[49] D. Gu, Y. Shen, G. Meng, Mater. Lett. 63 (2009) 2536-2538.
[50] J.W. Garvin, H.S. Udaykumar, J. Cryst. Growth 267 (2004) 724-737.
[51] L. Hadji, Scr. Mater. 48 (2003) 665-669.
[52] D. Gu, H. Zhang, D. Dai, M. Xia, C. Hong, R. Poprawe, Compos. B. Eng. 163 (2019) 585-597.
[53] L.-Y. Chen, J.-Q. Xu, H. Choi, M. Pozuelo, X. Ma, S. Bhowmick, J.-M. Yang, S. Mathaudhu, X.-C. Li, Nature 528 (2015) 539-543.
[54] W.-F. Ho, J. Alloys Compd. 464 (2008) 580-583.
[55] C.-C. Chung, S.-W. Wang, Y.-C. Chen, C.-P. Ju, J.-H. Chern Lin, Mater. Sci. Eng. A 631 (2015) 52-66.
[56] Y.-C. Chen, J.-H.C. Lin, C.-P. Ju, Mater. Des. (1980-2015) 54 (2014) 515-519.
[57] S. Dadbakhsh, R. Mertens, G. Ji, B. Vrancken, K. Vanmeensel, H. Fan, A. Addad, J.-P. Kruth, Addit. Manuf. 36 (2020) 101577.
[58] F. Akhtar, Can. Metall. Q. 53 (2014) 253-263.
[59] K.I. Parashivamurthy, R.K. Kumar, S. Seetharamu, M.N. Chandrasekharaiah, J. Mater. Sci. 36 (2001) 4519-4530.